

1 **Manuscript title:** The Integrated Voxel Analysis Method (IVAM) to Diagnose Onset of
2 Alzheimer’s Disease and Identify Brain Regions through Structural MRI Images.

3 **Authors/Affiliations:** Matthew Hur^{1,*}, Armen Aghajanyan²

4 ¹Yale University, New Haven, CT 06520. ²Facebook Research, Facebook Corporation, Menlo
5 Park, CA 94025. *Corresponding author.

6

7 **Abstract:** Magnetic Resonance Imaging (MRI) provides three-dimensional anatomical and
8 physiological details of the human brain. We describe the Integrated Voxel Analysis Method
9 (IVAM) which, through machine learning, classifies MRI images of brains afflicted with early
10 Alzheimer's Disease (AD). This fully automatic method uses an extra trees regressor model in
11 which the feature vector input contains the intensities of voxels, whereby the effect of AD on a
12 single voxel can be predicted. The resulting tree predicts based on the following two steps: a K-
13 nearest neighbor (KNN) algorithm based on Euclidean distance with the feature vector to classify
14 whole images based on their distribution of affected voxels and a voxel-by-voxel classification by
15 the tree of every voxel in the image. An Ising model filter follows voxel-by-voxel tree-
16 classification to remove artifacts and to facilitate clustering of classification results which identify
17 significant voxel clusters affected by AD. We apply this method to T1-weighted MRI images
18 obtained from the Open Access Series of Imaging Studies (OASIS) using images belonging to
19 normal and early AD-afflicted individuals associated with a Client Dementia Rating (CDR) which
20 we use as the target in the supervised learning. Furthermore, statistical analysis using a pre-labeled
21 brain atlas automatically identifies significantly affected brain regions. While achieving 90% AD
22 classification accuracy on 198 images in the OASIS dataset, the method reveals morphological
23 differences caused by the onset of AD.

24 **Introduction:** Alzheimer's Disease (AD) is a prevalent degenerative disorder in today's society
25 as the 7th leading cause of death in America (Speert et al., 2012). As the causes and inner
26 mechanisms underlying AD-related brain abnormalities are not fully understood, no cure has yet
27 been found; however, treatments such as pharmacology that inhibit acetylcholinesterase have
28 successfully prolonged the lifespan of affected individuals by slowing down the degeneration of
29 acetylcholine-releasing neurons (Bianchetti et al., 2006). Other biomolecular phenomena

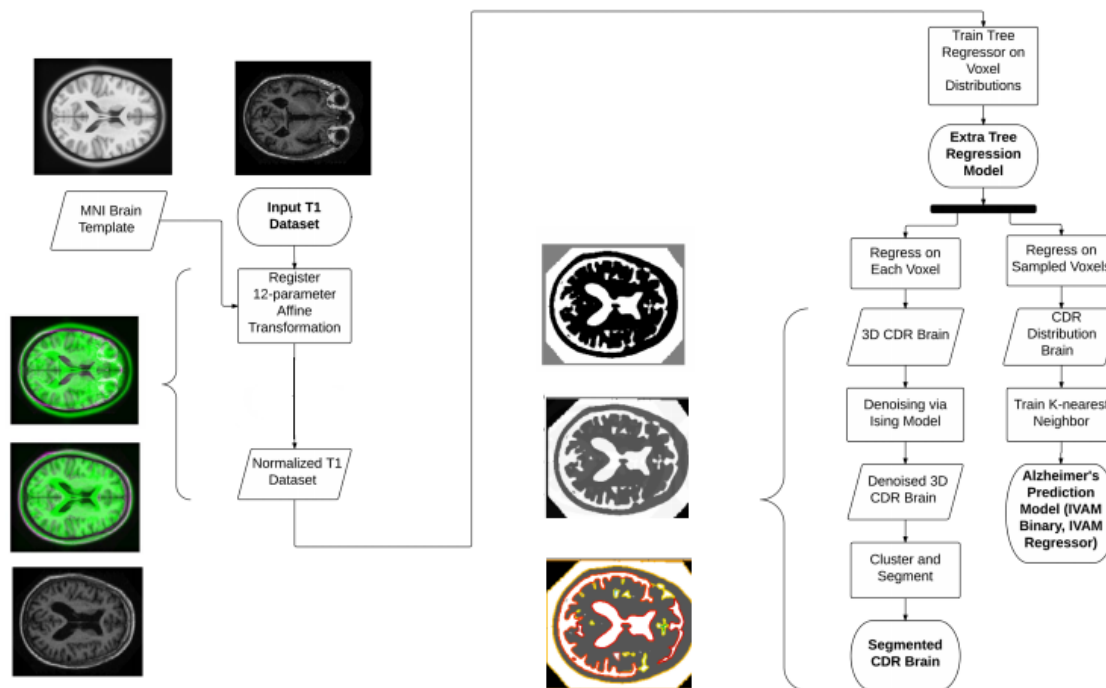
30 including the formation of beta-amyloid plaques and tau-fibrillary tangles have been implicated,
31 but its relation to macroscopic mechanisms concerning brain regions is still nebulous.
32 Computational methods for classification and segmentation can facilitate and supplement clinical
33 diagnoses.

34 In order to reveal these macroscopic mechanisms between brain regions, many current
35 image classification and segmentation algorithms incorporate an essential step of feature extraction.
36 For example, the widely used and effective Voxel-Based Morphometry (VBM) method is designed
37 for feature extraction to determine specific anatomic patterns of cerebral atrophy (Ashburner and
38 Friston, 2000). However, this method suffers from its dependence on a precise registration and
39 warping of MRI images to *a priori* probability maps (Veress et al., 2013). Its high sensitivity to
40 accurate registration creates a limitation because the templates inherently differ with various MRI
41 images due to structural variance of brain shape. Additionally, its high computational complexity
42 leads to complex implementation and long run-time. Other methods for segmentation such as the
43 Hybrid Watershed Algorithm (HWA) and the skull-stripping Brain Extraction Methods (BEM and
44 BEM2DE) rely on accurate iterative thresholding and on assumptions about brain shape that limit
45 their practical use when analyzing variegated brain shapes belonging to subjects of various
46 demographic groups (Fennema-Notestine et al., 2006). Fully automatic methods need to quickly
47 and effectively account for individual differences in brain shape without human supervision.

48 The essential steps that improve the results in these automatic methods are energy-based
49 deformation fields which identify regions of interest, whereby a driving force pushes an objective
50 function to convergence. Success of the energy methods can be attributed to the utilization of

51 information about local differences as well as about global trends of the image.

Integrated Voxel Analysis Method (IVAM)



52
53 Figure 1: A flowchart outlining the Integrated Voxel Analysis Method (IVAM) with cross-sections
54 resembling certain steps. The preprocessing step incorporates spatial normalization and (not shown)
55 skull-stripping to create a dataset applicable to sampling for IVAM. The machine learning section
56 utilizes a K-Nearest Neighbor (KNN) classifier which takes as input the voxel-by-voxel classified
57 brain from an extra-randomized regressor tree.

58 We propose a multifaceted algorithm that utilizes methods for decision-tree learning to
59 robustly and automatically classify AD affected brains as well as cluster and segment classification
60 results of individual voxels to yield severely affected brain regions (Figure 1). First, the method,
61 termed the Integrated Voxel Analysis Method (IVAM), skull-strips each test and training MRI
62 image and spatially normalizes to the MNI152 brain-masked, i.e. skull-stripped, template. At the

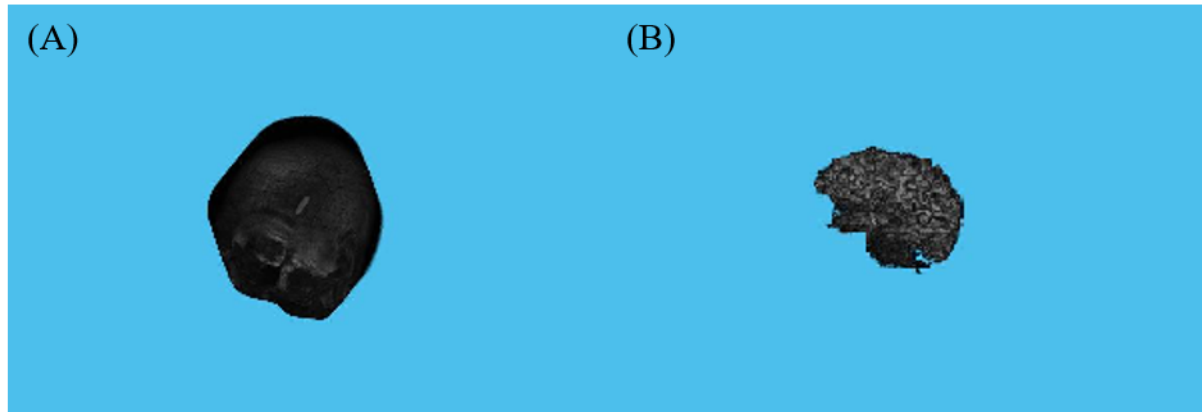
63 center of our framework of integrated processes is a trained extra-randomized trees regressor
64 known to be highly effective for supervised learning of complex data (Geurts et al., 2006). The
65 trained model is used to estimate the distribution of Alzheimer affected voxels, which are sampled
66 from the MRI. A second model placed on top of the distributions predicts the CDR of the whole
67 brain. The aggregated learning model can also automatically relay information about specifically
68 affected brain regions allowing for novel insights into the inner neurological workings of AD
69 tailored to accurately diagnose AD in its early stages.

70 **Methods:**

71 A. Data Set.

72 We obtain 233 anonymous MRI images from the Open Access Series of Imaging Studies
73 (OASIS) (Buckner et al., 2004). Their age range is from 18-96 years with a mean of 53 years with
74 each clinically diagnosed with a Client Dementia Rating (CDR) which rates subjects based on 6
75 criteria: memory, orientation, judgment and problem solving, function in the community, home
76 and hobbies, and personal care (Buckner et al., 2004). The values range from 0 to 3 where 0
77 indicates no dementia while 0.5 and 1 indicate very mild and mild dementia respectively. In order
78 to specifically analyze the onset of AD and due to the sparsity of the dataset of images labeled
79 with a $CDR > 1$, we use images labeled with a CDR of 0, 0.5, and 1. All images are T1-weighted
80 prepared rapid echo-gradient and obtained on a 1.5-T vision scanner by the OASIS study. (Buckner
81 et al., 2004). Acquisition matrix was [256 256] with 128 contiguous sagittal slices of thickness of
82 1.25 mm.

83 B. Skull-Stripping



84

85 Figure 2: (A) Left panel illustrates the raw rendering of the 3D image obtained from OASIS.

86 Right panel illustrates a brain with its skull image removed leaving behind gray and white

87 matter in the image.

88 We perform two gray-level thresholds on the raw MRI images using Matlab. Then, we

89 dilate the image with a ball structuring image, perform a third gray-level threshold, and isolate the

90 main part of the head by taking the largest connected component in 3D.

91 C. Spatial Normalization.

92 One of the most essential components to accurate analysis of MRI images is the spatial

93 normalization of the dataset. Through co-registration, processing of MRI images can be compared

94 across multiple subjects, especially important for brain Region of Interest (ROI) analysis in

95 pinpointing the affected regions. The images were normalized to the template provided by the

96 Montreal Neuroimaging Institute known as the MNI152 template built by averaging across 152

97 brains. The images were first converted to the same voxel resolution of 1mm x 1mm x 1mm and

98 symmetrically zero-padded to transform to the same dimensions. Next, each image was registered

99 to the MNI152 template using a one plus one evolutionary optimizer to maximize the mutual

100 information metric provided by David Mattes (Mattes et al., 2001).

101 D. Feature Selection

102 Feature selection algorithm relied on the assumption that the level of Alzheimer's projected
103 at a voxel depends on the surrounding voxels as well as the three-dimensional coordinate of the
104 voxel. Our feature vector included the values of all voxels around the voxel of interest with a preset
105 radius and the appended 3D coordinates of the voxels of interest as well as the gender of the subject
106 as male and female brain anatomy have been shown to exhibit structural differences (Ritchie *et al.*
107 2018). For each MRI image we enumerate all coordinates where the surrounding points are not all
108 zeros. For each voxel we selected features as described above. Because of the sheer size of MRI
109 images, we added a variable step constant throughout the whole aggregated model. Instead of
110 enumerating every point, the step dictates step incrementation in the coordinates for the voxel of
111 interest.

112 E. Building the Model.

113 The label of each feature vector is simply the CDR rating of respective patient. Once we
114 built the data-set, we randomly sampled half of the data and used that to train a the ensemble, Extra
115 Random Trees Regressor (Geurts et al., 2006) using the popular sklearn library (Pedregosa et al.,
116 2011). Although traditionally combined with an ensemble method such as Random Forests, these
117 Extra Random Tree Regressors (ERTR) tend to exhibit losses in accuracy observed through
118 computational trials we conducted compared to the ERTR alone. The ERTR now predicts the CDR
119 rating of single voxels in the MRI image.

120 F. Predicting the CDR.

121 Our method for predicting the CDR arises from our axiomatic assumption that the severity
122 of Alzheimer's disease in a patient, will be represented by the distribution of individual CDR

123 regressed voxels. Our first intuition was to use the Kullback-Leibler divergence as a tool to
124 compare the distributions. Although this gave us promising results, the utilization of K-Nearest
125 Neighbor (Bentley, 1975) achieved much greater accuracy than the Kullback-Leibler divergence.
126 Voxel sampling from the brain proceeded in the same way as feature selection, using the same
127 function. After sampling, the regression model predicted the CDR of each individual voxel. The
128 label or target for the KNN algorithm arises as a function of the CDR of the respective patient.
129 The accuracy will be introduced at the Discussion section below.

130 G. Identifying Severely Affected Brain Regions.

131 The process of pinpointing severely affected brain regions from MRI's can be seen as a
132 pipelining process. A sagittal half-brain slice of a normalized MRI image compares to the
133 following CDR classified image: the classified image depicts the results of the denoising model
134 applied to the CDR voxel predictions. Black, grey, and white correspond to CDR predictions of 0,
135 0.5, and 1 respectively.

136 H. Denoising via Ising Model

137 Using Murphy's derivation of the Ising model, we define the probability of the update as

$$138 \log \tilde{p}(\mathbf{y}) = - \sum_{s \neq t} y_s w_{st} y_t \quad (1)$$

139 (Murphy, 2012).

140 The weight w_{st} signifies the amount we attribute to the difference between the two pixels
141 from each 2D slice and y_n represents the intensity value of voxel y . To simplify the calculations,
142 we modify our equation to:

$$143 \log \tilde{p}(\mathbf{y}) = \frac{1}{2} \mathbf{y}^T \mathbf{W} \mathbf{y} \quad (2),$$

144 where W is a Toeplitz matrix. We define our objective function as

145
$$\operatorname{argmax} p(y, x) = p(x)p(y|x) \quad (3).$$

146 Continuing, by Murphy's derivation, the unnormalized prior develops as follows:

147
$$p(x) = \frac{1}{Z_0} e^{-E_0(x)} = \frac{1}{Z_0} e^{\sum_i \sum_{j \in \text{nbhd}(i)} W_{ij} x_i x_j} \quad (4),$$

148 where nbhd denotes the immediate neighborhood of the two-dimensional pixel j . The Z_0 is not

149 needed since we are using the unnormalized prior. On the other hand, our unnormalized posterior

150 will be:

151
$$p(x|y) = \frac{p(y|x)p(x)}{p(x,y)} = \frac{1}{Z} e^{\sum_i L_i(x_i) - E_0(x)} \quad (5).$$

152 For the mean field update, we need to compute (see Murphy section 21.3.1 for details)

153
$$\log q_j(x_j) = E_{-q_j} [\log \tilde{p}(x)] + \text{const} \quad (6).$$

154 and since

155
$$E_{-q_j}(f) = \sum_{k \neq j} q(x_k, \mu_j | x_j) f(j) = \sum_{k \neq j} q(\mu_j) f(j) \quad (7),$$

156 we have

157
$$q_i(x_i) \propto e^{x_i \sum_{j \in \text{nbhd}} W_{ij} \mu_j + L_i(x_i)} \quad (8).$$

158 which yields the important theoretical step. Murphy derives an actual update. In Murphy's

159 (Murphy, 2012) derivation (page 738), note that it uses

160
$$L + i \equiv L_i(+1) \text{ and } L - i \equiv L_i(-1) \quad (9).$$

161 which are the log likelihood functions centered at each of these two values. The variance in the
162 likelihood controls the strength of the prior. This is the final update, which also incorporates a
163 damping term:

$$164 \quad \mu_i^t = (1 - \lambda)\mu_i + \lambda \tanh(x_i \sum_{j \in nbhd} W_{ij}\mu_j + 0.5(L_i^+ - L_i^-)) \quad (10)$$

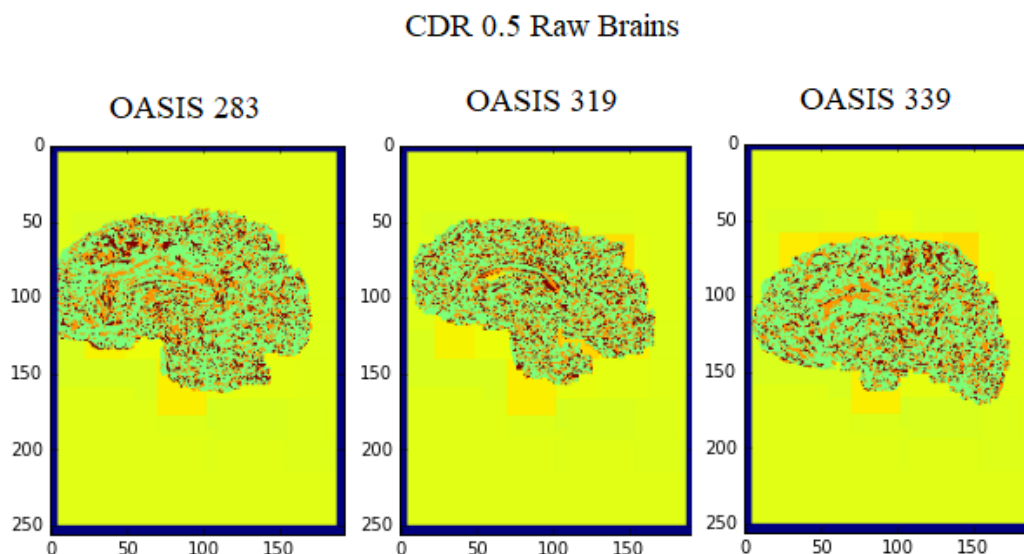
165 To convert this algorithm into a tertiary denoiser, we introduced this function to convert CDR to
166 Ising denoiser values,

$$167 \quad (2 * CDR) - 1 \quad (11).$$

168 I. Clustering and Segmentation Model.

169 Our clustering and segmentation model bases on Ward's method (Ward, 1963). We input
170 the connectivity matrix of the denoised image into Ward's hierarchical clustering method. The
171 connectivity matrix can be defined as a matrix where each sample is defined through the
172 neighboring samples following a given structure of the data. The connectedness structure of the
173 data consisted of the one-voxel neighborhood of each voxel.

174 **Results:**



175

176 Figure 3: Shown are three sagittal cross-sections of brains afflicted by Alzheimer's Disease with
177 a CDR of 0.5. Two brains show high severity near the hippocampus while all three show moderate
178 to severe severity near the inferior sagittal sinus. OASIS 339 illustrates how many brains afflicted
179 by Alzheimer's Disease show severity near the cortices separating brain lobes.

180 The hippocampus, heavily involved in memory storage, appears highly affected at both 0.5
181 and 1.0 CDR according to IVAM. In a sagittal cross-section, the streak above the hippocampus
182 known as the inferior sagittal sinus appears slightly less but still highly affected by early
183 Alzheimer's Disease.

184 To automate the finding of affected brain regions, we downloaded the Talairach labeled
185 database and registered it to the MNI template, then through a series of 90 degree 3D rotations,
186 matched it to the orientation of 3D classified brains. Testing the difference between brain regions
187 of CDRs of 0 (n = 51) and 0.5 (n = 11), the results are shown in Table 1.

Table 2: Significances between brains with CDR of 0 (n = 51) and 0.5 (n = 11).		
	Region Name	p-value
1	'Left Cerebrum.Limbic Lobe.Inferior Temporal Gyrus.White Matter.*'	0.047568
2	'Left Cerebrum.Frontal Lobe.*.*.*'	0.041913
3	'Right Cerebrum.Frontal Lobe.*.*.*'	0.035739
4	'Left Cerebellum.Anterior Lobe.Pyramis.Gray Matter.*'	0.010867
5	'Right Cerebrum.Limbic Lobe.Fusiform Gyrus.Gray Matter.Brodmann area 20'	0.025399
6	'Right Cerebrum.Limbic Lobe.Fusiform Gyrus.White Matter.*'	0.027071
7	'Right Cerebrum.Frontal Lobe.Orbital Gyrus.Gray Matter.Brodmann area 47'	0.045191
8	'Right Cerebrum.Frontal Lobe.Middle Frontal Gyrus.*.*'	0.00947
9	'Left Cerebrum.Limbic Lobe.Parahippocampal Gyrus.Gray Matter.Amygdala'	0.037748
10	'Left Cerebrum.Frontal Lobe.Medial Frontal Gyrus.*.*'	0.03215
11	'Left Cerebrum.Occipital Lobe.Fusiform Gyrus.Gray Matter.Brodmann area 19'	0.032959
12	'Left Cerebrum.Frontal Lobe.Subcallosal Gyrus.*.*'	0.02893
13	'Right Cerebrum.Frontal Lobe.Subcallosal Gyrus.White Matter.*'	0.042401
14	'Right Cerebrum.Frontal Lobe.Subcallosal Gyrus.Gray Matter.Brodmann area 47'	0.028412
15	'Right Cerebrum.Occipital Lobe.Middle Occipital Gyrus.*.*'	0.043875
16	'Right Cerebrum.Occipital Lobe.Parahippocampal Gyrus.Gray Matter.Brodmann area 37'	0.018895
17	'Left Cerebrum.Sub-lobar.Third Ventricle.Cerebro-Spinal Fluid.*'	0.021665
18	'Right Cerebrum.Temporal Lobe.Sub-Gyral.Gray Matter.Brodmann area 13'	0.035569
19	'Left Cerebrum.Frontal Lobe.Extra-Nuclear.*.*'	0.045111
20	'Right Cerebrum.Frontal Lobe.Superior Frontal Gyrus.Gray Matter.Brodmann area 10'	0.047755
21	'*.*.Sub-Gyral.*.*'	0.049801
22	'Right Cerebrum.Sub-lobar.Caudate.Gray Matter.Caudate Head'	0.025211
23	'Right Cerebrum.Sub-lobar.Inferior Frontal Gyrus.Gray Matter.Brodmann area 47'	0.006871
24	'Right Cerebrum.Frontal Lobe.*.Gray Matter.Brodmann area 10'	0.034613
25	'Right Cerebrum.Occipital Lobe.Inferior Temporal Gyrus.Gray Matter.Brodmann area 18'	0.043662
26	'Right Cerebrum.Midbrain.Extra-Nuclear.White Matter.*'	0.025544
27	'Left Cerebrum.Frontal-Temporal Space.Superior Temporal Gyrus.*.*'	0.049101
28	'Right Cerebrum.Frontal Lobe.Sub-Gyral.Gray Matter.Brodmann area 10'	0.027311
29	'Right Cerebrum.*.Cuneus.Gray Matter.*'	0.003708
30	'Right Cerebrum.Temporal Lobe.Lingual Gyrus.Gray Matter.Brodmann area 19'	0.033767

31	'Right Cerebrum.Temporal Lobe.Superior Temporal Gyrus.Gray Matter.*'	0.007284
32	'Right Cerebrum.Sub-lobar.Extra-Nuclear.White Matter.Medial Globus Pallidus'	0.000862
33	'Left Cerebrum.Sub-lobar.Inferior Frontal Gyrus.Gray Matter.Brodmann area 47'	0.017253
34	'Left Cerebrum.Sub-lobar.Thalamus.Gray Matter.Pulvinar'	0.04674
35	'Left Cerebrum.Sub-lobar.Inferior Frontal Gyrus.*.*'	0.037133
36	'Left Cerebrum.Limbic Lobe.Posterior Cingulate.Gray Matter.Brodmann area 30'	0.026286
37	'Left Cerebrum.Occipital Lobe.Middle Temporal Gyrus.Gray Matter.Brodmann area 19'	0.0116
38	'Right Cerebrum.Occipital Lobe.Middle Temporal Gyrus.Gray Matter.Brodmann area 39'	0.046534
39	'Right Cerebrum.Temporal Lobe.Superior Temporal Gyrus.Gray Matter.Brodmann area 39'	0.035883
40	'Left Cerebrum.Temporal Lobe.Transverse Temporal Gyrus.Gray Matter.Brodmann area 41'	0.009321
41	'Left Cerebrum.Sub-lobar.Transverse Temporal Gyrus.Gray Matter.Brodmann area 41'	0.009155
42	'Left Cerebrum.Sub-lobar.Thalamus.Gray Matter.Lateral Posterior Nucleus'	0.005067
43	'Right Cerebrum.Temporal Lobe.Precentral Gyrus.White Matter.*'	0.031295
44	'Left Cerebrum.Frontal Lobe.Insula.White Matter.*'	0.046733
45	'Left Cerebrum.Limbic Lobe.Extra-Nuclear.*.*'	0.030946
46	'Inter-Hemispheric.Limbic Lobe.Anterior Cingulate.*.*'	0.020917
47	'Left Cerebrum.*.Middle Frontal Gyrus.*.*'	0.005934
48	'Left Cerebrum.Limbic Lobe.Posterior Cingulate.Gray Matter.*'	0.013244
49	'Right Cerebrum.Limbic Lobe.Posterior Cingulate.Gray Matter.*'	0.032718
50	'Right Cerebrum.Parietal Lobe.Precentral Gyrus.*.*'	0.030813
51	'Left Cerebrum.Frontal Lobe.Inferior Frontal Gyrus.Gray Matter.Brodmann area 6'	0.045349
52	'Left Cerebrum.*.Inferior Frontal Gyrus.*.*'	0.022252
53	'Right Cerebrum.Occipital Lobe.Precuneus.Gray Matter.Brodmann area 18'	0.029092
54	'Left Cerebrum.Occipital Lobe.Superior Occipital Gyrus.Gray Matter.Brodmann area 19'	0.033095
55	'Right Cerebrum.Temporal Lobe.Cuneus.White Matter.*'	0.017632
56	'Right Cerebrum.Temporal Lobe.Inferior Parietal Lobule.*.*'	0.04041
57	'Right Cerebrum.Parietal Lobe.Inferior Parietal Lobule.*.*'	0.026267
58	'Right Cerebrum.Parietal Lobe.Postcentral Gyrus.Gray Matter.Brodmann area 3'	0.048072
59	'Inter-Hemispheric.*.Superior Frontal Gyrus.*.*'	0.026462
60	'Right Cerebrum.Frontal Lobe.Inferior Parietal Lobule.White Matter.*'	0.010282

61	'Right Cerebrum.Limbic Lobe.Medial Frontal Gyrus.*.*'	0.038014
62	'Left Cerebrum.Occipital Lobe.Angular Gyrus.*.*'	0.041118
63	'Right Cerebrum.Occipital Lobe.Angular Gyrus.*.*'	0.029264
64	'Left Cerebrum.Parietal Lobe.Precuneus.Gray Matter.Brodmann area 39'	0.040566
65	'Left Cerebrum.Parietal Lobe.Angular Gyrus.Gray Matter.Brodmann area 40'	0.041285
66	'Right Cerebrum.Parietal Lobe.Sub-Gyral.Gray Matter.Brodmann area 40'	0.049041
67	'Left Cerebrum.Frontal Lobe.Sub-Gyral.Gray Matter.Brodmann area 6'	0.044811
68	'Right Cerebrum.Frontal Lobe.Superior Frontal Gyrus.Gray Matter.Brodmann area 8'	0.027852
69	'Left Cerebrum.Parietal Lobe.Superior Parietal Lobule.*.*'	0.028557
70	'Right Cerebrum.Parietal Lobe.Superior Parietal Lobule.Gray Matter.Brodmann area 7'	0.048063
71	'Left Cerebrum.Frontal Lobe.Paracentral Lobule.*.*'	0.006011
Table 2: Significances between brains with CDR of 0 (n = 24) and 1 (n = 8).		
	Brain Region	P-Value
1	'Right Cerebrum.Temporal Lobe.Insula.Gray Matter.*'	0.019939
2	'Left Cerebrum.Frontal Lobe.Middle Frontal Gyrus.Gray Matter.*'	0.037358
3	'Right Cerebrum.Sub-lobar.Inferior Frontal Gyrus.Gray Matter.Brodmann area 45'	0.045422
4	'Left Cerebrum.Sub-lobar.Transverse Temporal Gyrus.White Matter.*'	0.015406
5	'Right Cerebrum.Temporal Lobe.Transverse Temporal Gyrus.Gray Matter.Brodmann area 42'	0.018149
6	'Right Cerebrum.Limbic Lobe.Posterior Cingulate.Gray Matter.Brodmann area 31'	0.031017
7	'Left Cerebrum.Limbic Lobe.Posterior Cingulate.Gray Matter.Brodmann area 18'	0.040112
8	'Left Cerebrum.Parietal Lobe.Postcentral Gyrus.*.*'	0.036241
9	'Left Cerebrum.Parietal Lobe.Postcentral Gyrus.Gray Matter.*'	0.049764
10	'Left Cerebrum.Frontal Lobe.Postcentral Gyrus.Gray Matter.Brodmann area 4'	0.040556
11	'Right Cerebrum.Parietal Lobe.Postcentral Gyrus.Gray Matter.Brodmann area 3'	0.034089
12	'Right Cerebrum.Occipital Lobe.Cuneus.Gray Matter.Brodmann area 31'	0.019641
13	'*.*.Angular Gyrus.*.*'	0.031262
14	'Left Cerebrum.Parietal Lobe.Sub-Gyral.Gray Matter.Brodmann area 2'	0.035837
15	'Left Cerebrum.Parietal Lobe.Superior Parietal Lobule.*.*'	0.049594
16	'Right Cerebrum.Parietal Lobe.Paracentral Lobule.Gray Matter.Brodmann area 5'	0.037892
17	'Right Cerebrum.Parietal Lobe.Postcentral Gyrus.Gray Matter.Brodmann area 5'	0.015352

189 **Conclusion:**

190 We created the best performing algorithm to-date for classifying 3D images taken of
191 patients of neurodegenerative and neuropsychiatric diseases. In addition, the accuracy for voxel-
192 by-voxel classification hovers around 83% as we labeled each voxel with the CDR of the brain.
193 These diseases and disorders exhibit classification through many types of benchmarks that rate
194 their severity. The IVAM code can be easily modified to accommodate different rating scales.

195 **Discussion:**

196 The skull-stripping algorithm we developed performs extremely well visually as shown for
197 a single MRI image (Figure 2) separating the cortices from the skull as well as the cerebellum and
198 lower brain from the skull in most instances. It performed successfully on a lot of the 380 images.
199 There are examples of a missing lower brain, but nevertheless the algorithm achieved up to 90.0%
200 classification accuracy. Adjustment of the dimensions of the structuring element could improve
201 the results as well as a more robust thresholding algorithm such as a modified IsoData algorithm.
202 A previously running version of IVAM which ran on spatially normalized images performed by
203 OASIS authors but not skull-stripped by us achieved 92.2%. These data were pre-processed as a
204 non-linear warping to the MNI152 template by OASIS authors.

205 After running IVAM on nearly 200 images in the OASIS dataset, we find that a single
206 extra-randomized tree regressor predicts with 90.0% accuracy when trained on around 90% of the
207 dataset and tested on around 10% of the dataset, which represents the highest accuracy reported
208 to-date on structural MRI images of Alzheimer's Disease patients, as a tertiary regression on CDRs
209 of 0, 0.5, and 1 in early AD and 83.3% accuracy as a binary regression of 0 and any higher CDR.
210 We also find that the extra-randomized trees regressor as a forest (a bag of trees) predicts with

211 89.7% accuracy as a tertiary regression and 83.8% accuracy as a binary regression. We found that
212 the single extra-randomized regressor tree predicts better than a bag of them. Current state-of-the-
213 art prediction methods include a maximum of around 85% in binary classification as explained by
214 Moscoso *et al.* 2019.

215 Next steps include improving the KNN part of the algorithm to accept non-integer values,
216 i.e. CDR of 0.5, which should theoretically yield higher accuracy than the current tertiary
217 classification, and improving identification of severely affected areas to a probabilistic map using
218 the labeled MNI152 atlas which can be retrieved by installing MindBoggle.

219 **Acknowledgements:**

220 We would like to thank Dr. Nigel S. Bamford for giving critiques on the performance of our
221 algorithm and reviewing our writing.

244 Mattes, D., David, H., Vessele, H., Lewellyn, T., and Eubank, W. (2001). Nonrigid multimodality
245 image registration. *Medical Imaging*. Murphy, K. P. (2012). *Machine learning: a probabilistic*
246 *perspective*. Cambridge, MA.

247 Moscoso, A., Silva-Rodriguez J., Aldrey M., J., Cortes, J., Fernandez-Ferreiro A., Gomez-Lado,
248 N., Ruibal, A., Aguiar, P. (2019). Prediction of Alzheimer’s disease dementia with MRI beyond
249 the short-term: Implications for the design of predictive models. *Neuroimage Clin.* 23: 101837

250 Pedregosa, F., Varoquaux, G., Gramfort, A., Michel, V., Thirion, B., Grisel, O., Blondel, M.,
251 Prettenhofer, P., Weiss, R., Dubourg, V., Vanderplas, J., Passos, A., Cournapeau, D., Brucher, M.,
252 Perrot, M., and Duchesnay, E. (2011). Scikitlearn: Machine learning in Python. *Journal of Machine*
253 *Learning Research*, 12:2825–2830.

254 Scholkopf, B. and Smola, A. J. (2002). *Learning with kernels*. MIT Press.

255 Speert, D., Benson, T., Cameron, J., Kaplan, B., Parfitt, D., and Roskams, A. J. (2012). *BrainFacts*
256 *A Primer on the Brain and Nervous System*. Society for Neuroscience.

257 Veress, A. I., Klein, G., and Gullberg, G. T. (2013). A comparison of hyperelastic warping of pet
258 images with tagged mri for the analysis of cardiac deformation. *Int. J. Biomedical Imaging*, 2013.

259 Ward, J. H. (1963). Hierarchical grouping to optimize an objective function. *Journal of the*
260 *American Statistical Association*, 58(301):236–244